PNAS RESEARCH ARTICLE | EARTH, ATMOSPHERIC, AND PLANETARY SCIENCES

Anatomy of the magmatic–hydrothermal system beneath Uturuncu volcano, Bolivia, by joint seismological and petrophysical analysis

Ying Liu[a,b], John Michael Kendall[c,1], Haijiang Zhang[a,b,1], Jonathan D. Blundy[c], Matthew E. Pritchard[d], Thomas Hudson[c,2], and Patricia MacQueen[d,3]

Affiliations are included on p. 9.

Edited by Katharine Cashman, University of Oregon, Eugene, OR; received October 12, 2024; accepted February 26, 2025

For a volcanic system, evaluating potential eruption probability requires understanding the extent of melt and gas accumulation in the upper crustal reservoir, which is challenging to resolve. Here, we jointly use geophysical imaging and petrophysical analysis to unravel the current state and pathway of gas or supercritical fluids in the upper crust beneath Uturuncu volcano in Bolivia. Although it last erupted 250 ± 5 ka ago, Uturuncu remains active with observable deformation and seismicity. To assess its current state, we have determined high-resolution isotropic and anisotropic seismic velocity structures of the volcanic system in the upper crust using local seismic networks. Combining our seismic analysis with previous geophysical imaging results and rock physics modeling, we delineate pathways of migrating fluids traveling toward the surface and a shallow gas accumulation zone beneath the crater. This fluid migration and accumulation explains why Uturuncu volcano still shows signs of activity. Our study exemplifies how seismology combined with rock physics models and petrological analysis can resolve the detailed structure and composition of a volcanic system, critical for assessing eruption hazard.

Uturuncu volcano | magmatic–hydrothermal system | seismic tomography | petrology and rock physics analysis | fluid and gas concentrations

Significance

Assessing the onset, duration, and magnitude of potential volcanic eruptions requires the characterization of the spatial concentrations of melt and gas in the upper crust of a volcano. In this study, we demonstrate how combining seismology, petrology, and rock physics can reveal the internal structure and composition of the hydrothermal system, especially mapping the migration pathways of fluids and gases beneath Uturuncu volcano. Based on the characterization of the magmatic-hydrothermal system beneath Uturuncu, we deduce that it is currently at low eruption risk. This comprehensive approach not only explains why a "zombie" volcano remains active but also offers insights into its eruption potential, establishing a technique that could be applied to help evaluate eruption hazards at other active volcanoes.

Magmatic systems in the crust are dominated by crystal mush and usually involve transcrustal processes (1, 2). Magma reservoirs in the lower crust can be long-lived, producing evolved melts that are enriched in volatiles and incompatible elements by melt segregation and fractionation, which can ascend to shallower regions in the crust. Mainly due to an abrupt increase in rigidity at the brittle-ductile transition (BDT), ascending melts commonly accumulate in the middle crust to form another magma reservoir, which further supplies magma for upper crustal magma chambers. Through magma decompression, volatile exsolution can occur, leading to the accumulation of volatiles at the chamber roof. These volatiles may segregate to form an isolated volatile layer or migrate to feed an overlying hydrothermal system, both of which play an important role in the dynamics of magmatic systems.

Huppert and Woods (3) demonstrated that volcanic eruptions can potentially increase in duration and magnitude by up to two orders of magnitude if the internal energy stored with dissolved volatiles is released into the magma storage regions, especially in cases where storage regions are shallow (where volatile solubility is low) or magmas are rich in dissolved volatiles. Seismic tomography methods have been used to characterize the transcrustal magmatic systems (4–7), however, most studies mainly focused on resolving individual magma reservoirs. Only a few seismic tomography studies have endeavored to understand the interactions between magmatic reservoirs and overlying hydrothermal systems (8–10). However, these studies neither characterize the full image of volatile pathways nor give a quantitative estimate of volatile concentrations for magmatic–hydrothermal systems. In this study, we unravel the architecture of the magmatic–hydrothermal system of the Uturuncu volcano in southern Bolivia near the Chile–Argentina border by integrating multiple geophysical imaging results and petrophysical analysis.

Uturuncu is a rear arc volcano in the Central Andes resulting from subduction of the oceanic Nazca plate beneath the South American continental plate (Fig. 1). Uturuncu itself is a Pleistocene-age volcano composed exclusively of approximately 50 km^3 of homogeneous, porphyritic dacite lava flows (62 to 67 wt% SiO_2) erupted between 1,060 and 250 ka (11).

Uturuncu sits above the world's largest body of silicic partial melt, known as the Altiplano–Puna magma body (APMB) (14, 15), and lies within the APVC, a major volcano-tectonic province formed by a large volume (>15,000 km^3) ignimbrite flare-up between 11 and 1 Ma (12). The existence of the APMB below the APVC is evidenced

This article is a PNAS Direct Submission.

[1]To whom correspondence may be addressed. Email: mike.kendall@earth.ox.ac.uk or zhang11@ustc.edu.cn.

[2]Present address: Department of Earth and Planetary Sciences, ETH Zurich, Zurich 8092, Switzerland.

[3]Present address: Geology, Geophysics, and Geochemistry Science Center, United States Geological Survey, Denver, CO 80225-0046.

This article contains supporting information online at https://www.pnas.org/lookup/suppl/doi:10.1073/pnas.2420996122/-/DCSupplemental.

Published April 28, 2025.

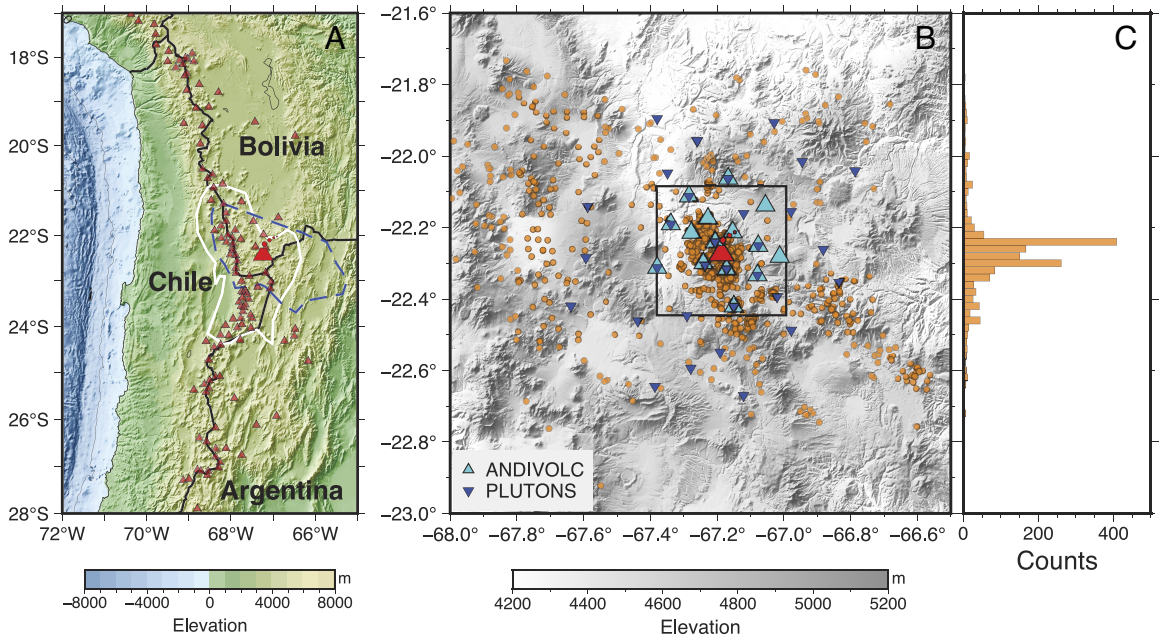

Fig. 1. Geological context of Uturuncu volcano. (*A*) Distribution of Holocene volcanoes (from Global Volcanism Program, 2024. [Database] Volcanoes of the World (v. 5.2.2; 22 Aug 2024). Distributed by Smithsonian Institution, compiled by Venzke, E. https://doi.org/10.5479/si.GVP.VOTW5-2024.5.2) are shown in red triangles. The summit of Uturuncu is marked as a larger red volcano symbol. The outlines of the Altiplano–Puna volcanic complex (APVC) from ref. 12 and Altiplano–Puna magma body from ref. 13 are shown in white solid and blue dashed lines respectively. (*B*) Distribution of seismic events and stations. Cyan triangles and blue inverted triangles denote seismic stations of ANDIVOLC and PLUTONS networks, respectively. The summit of Uturuncu is marked with a red volcano symbol. (*C*) Histogram of relocated seismic events along latitude direction in bins of 0.02°.

and constrained by independent geophysical properties, including low seismic velocities (13, 16), low density (17), and low electrical resistivity (18). A velocity model obtained from joint inversion of ambient noise surface wave dispersion data and P-wave receiver functions suggests that the APMB is located at 4 to 25 km depth below sea level (bsl) and extends over a vast volume of ~500,000 km^3 with a diameter of ~200 km (16). By utilizing inversion of Bouguer gravity anomaly data, (17) revealed vertically elongated low-density anomalies rooted at the top of APMB and suggested that silicic magmas in the hot ductile mid-upper crust ascend diapirically from the APMB. Recent focused gravity observations on Uturuncu itself reveal a shallow, high-density structure that could be related to a shallow dacitic pluton or ore body (19). An electrical resistivity model, obtained by three-dimensional (3D) inversion of magnetotelluric data, shows that there are low-resistivity pathways (or "tendrils") connecting the APMB to the surface below Uturuncu (20). In addition, geochemical analysis shows that the erupted dacite lava flows are related genetically to water-rich andesite magmas which are postulated to originate within the APMB (11, 21, 22). Radiogenic isotopic studies indicate that dacite petrogenesis involves a significant contribution from partial melting of the Andean crust (23). Residues from partial melting may be represented by rare metapelitic gneiss xenoliths within the dacite lavas (22).

Although its last eruption took place 250 ± 5 ka ago (11), Uturuncu is sometimes referred to as a "zombie" volcano due to its ongoing noneruptive activity revealed through multidisciplinary investigations. Geodetic studies have detected a region of deformation with a width of approximately 150 km centered approximately 3 km to the southwest of Uturuncu's summit (15, 24–26). This deformation signal exhibits a "sombrero" pattern with central uplift and surrounding subsidence, which some authors attribute to magmatic processes in the middle to lower crust [e.g., (24)]. The central uplift, which has lasted for at least 50 y (27), occurs at variable rates of up to 1 cm/y with subdecadal fluctuations and recent deceleration (25, 28, 29).

Seismicity is another sign of the unrest beneath Uturuncu (30–32). Taking advantage of the abundant seismicity, several different seismological investigations have been conducted. The dominant NW-SE-oriented fast directions from shear wave splitting analysis reflect the influence of preexisting faults on the shallow stress state (32). Analysis of earthquake moment magnitudes suggests the b-values of shallow seismicity at Uturuncu are >1; these earthquakes are interpreted as fluid-enhanced seismicity (30). Seismic velocity structures in the crust have also been studied using receiver functions (14, 33), body wave tomography (13, 34–36), and ambient noise surface wave tomography (16).

Due to the sparse distribution of surface seismic stations, previous studies focused mainly on the velocity structure in the upper-middle crust, with the limited resolution at depths shallower than ~15 to 20 km. Some studies suggest the existence of an active hydrothermal system within the upper 10 km [e.g., (30, 31, 37)]. However, what drives this activity is uncertain, yet critical to understanding the shallow temperature and rheological structure. Understanding the drivers of this activity is thus a primary focus of this work. The crust in the upper 10 km is seismically active with triggered earthquakes, non-double-couple earthquakes, and earthquake swarms (30, 31, 37) and is associated with a low seismic velocity zone (31), and an unusual set of EW, interfingered zones of high and low resistivity each with a volume of ~500 km^3 (20). To unravel the origin of the shallow hydrothermal system activity beneath Uturuncu, especially how gases migrate upward from the APMB to the surface, we performed high-resolution 3D isotropic and anisotropic tomography using body wave arrival times of more than 1,700 events recorded by two local seismic networks. The determined high-resolution isotropic and anisotropic velocity structures revealed in our tomographic models shed light on the shallow hydrothermal system of Uturuncu above 5 km bsl. To further understand the hydrothermal system, we further estimated the melt and gas saturation state using rock physics modeling. See *SI Appendix* for details about the dataset, tomographic procedures, in situ Vp/Vs measurements, and rock physics modeling.

Results

We assembled seismic records for the period of April 2009 to October 2012 from two networks (48 stations in total, Fig. 1), ANDIVOLC and PLUTONS, to perform seismic velocity tomography at Uturuncu volcano (*SI Appendix*, Figs. S1 and S2). Compared to previous studies that only determine Vp and Vs structures (34), here we focus on Vp/Vs and azimuthal anisotropy structures that are more sensitive to the lithology, fluids, and deformation. In contrast to conventional methods, the newly developed Vp/Vs consistency-constrained double-difference (DD) tomographic technique makes use of absolute arrival times and differential S-P travel times to directly constrain the Vp/Vs structure with comparable resolution to the simultaneously determined Vp and Vs structures (38). As it exploits differential travel times of event pairs that have similar ray paths outside the source region, the DD tomography method can produce finer images in the source region (39), and is therefore suited to unveiling the detailed structures of the shallow hydrothermal system. Besides the differential travel times constructed from the absolute travel time catalog, the waveform cross-correlation (WCC) differential travel times of event pairs are also calculated and used to improve the accuracy of earthquake relocations and inverted velocity models (*SI Appendix*, Figs. S3–S6). After obtaining isotropic velocity models (Vp, Vs, and Vp/Vs) using DD seismic tomography, we further determined the P-wave azimuthal anisotropic model using the P-wave travel time anisotropic tomography technique (40, 41). According to the results of the checkerboard test, both isotropic velocity models (Vp, Vs, and Vp/Vs) and azimuthal anisotropic models (fast directions and anisotropic strength) in the vicinity of the volcano summit are well resolved with lateral resolutions of up to 2.5 and 5.0 km, respectively (*SI Appendix*, Fig. S7). The model restoration tests also show that the main features in our isotropic and anisotropic models are reliable (*SI Appendix*, Fig. S8).

According to the relocations obtained by the DD method, seismicity at Uturuncu is concentrated around the summit within 5 to 10 km distance laterally except for the NW-SE trending cluster in the southeast margin (Fig. 2*A*). As seismic events in the later cluster all occurred during local daytime (8:00 am to 6:00 pm), they are probably related to mine operations rather than the activity beneath the volcano. The distribution of seismicity around the summit shows a right semicircle pattern in map view with most events located to the east and north of the summit at depths around 0 km bsl. Viewed in a vertical cross section, the seismicity distribution defines a broad dome with its apex beneath the summit, in agreement with (30) who relocated those events using the NonLinLoc method based on the STA/LTA picked catalog that has fewer S wave arrivals. The map view of velocity structures at depths of 2.5 km above sea level (asl) and 0 km bsl shows a circular pattern with high Vp, high Vs, low Vp/Vs, and low azimuthal anisotropy near the summit surrounded by large low Vp, low Vs, high Vp/Vs, and high azimuthal anisotropy anomalies with NNW-SSE trends (Fig. 3 *A* and *B*). In vertical sections across the summit, a distinct column of high Vp/Vs rises from ~ 10 km bsl through a region of otherwise low Vp/Vs toward the summit. Around sea level, this column switches to a low Vp/Vs region surrounded by high Vp/Vs (Fig. 3 *C* and *D*). The strength of azimuthal anisotropy is extremely low at depths below sea level, whereas a region of high azimuthal anisotropy is distributed in a hat-like pattern above the seismicity at ~0 km bsl. Two dominant fast directions are observed in the rose diagram: NW-SE and NE-SW (Fig. 2*B*). To verify the velocity structure determined using seismic tomography, we further estimated the in situ Vp/Vs of compact seismicity clusters around the summit by using the WCC P-wave and S-wave differential times following the method developed by (42) (*SI Appendix*). Both in situ Vp/Vs measurements and the average Vp/Vs values interpolated from the 3D tomographic Vp/Vs model show that the shallow seismicity at Uturuncu occurred in low Vp/Vs regions (~1.55 to 1.65, Fig. 2*C* and *SI Appendix*, Figs. S9–S11).

Discussion

Pathway of Gas or Supercritical Fluids From APMB. The APMB beneath Uturuncu is well resolved and constrained by multidisciplinary studies, which is characterized by low seismic velocity (13, 14, 16, 33, 34), low resistivity (18), and low density (17). Although the depth range of the APMB varies among different studies because of the different sensitivities of different geophysical techniques to the presence, composition, amount, and distribution of partial melting, there is consensus that the APMB is a source of the deformation signal at Uturuncu (15, 43). However, it remains unclear how this deformation is transmitted from the middle crust to the surface. (34) detected a tooth-shaped high Vp/Vs column that grows from greater depths (at ~ 80 km) to the shallow crust and stops at ~ 2 km bsl. However, in their model, the features with horizontal scales less than 15 km are not well resolved as only the PLUTONS dataset is used. In contrast, our results with higher resolution show a thin vertical column in the Vp, Vs, and Vp/Vs models (Fig. 3 *C* and *D*), suggesting a pathway of gas or supercritical fluids from the APMB toward the surface, which has also been inferred from time-dependent gravity observations (44). This columnar anomaly stops at around sea level, coinciding with the onset of seismicity, which we attribute to the BDT. The depth and dome-shaped topography of the local shallow BDT, as inferred from the relocated earthquakes, align with the findings in ref. 30. This is also consistent with the sensitivity of the BDT to temperature, which is elevated by ascending hot fluids from the APMB.

Shear wave splitting analysis at Uturuncu reveals two dominant fast directions (NW-SE and NE-SW), which are associated with the preexisting faults distributed in both directions (30, 32). These studies attributed the fault-parallel orientations to crack opening and alignment along the fault strike due to perturbation of the shallow stress state caused by magma unrest or fluid migration. However, shear wave splitting results only provide integrated azimuthal anisotropy along raypaths. In comparison, P-wave azimuthal anisotropy tomography unravels the 3D distribution of the fast direction and its strength of azimuthal anisotropy in the shallow crust. From the map view of the azimuthal anisotropy structures, at 0 km bsl the low anisotropy directly beneath Uturuncu is surrounded by a circular region of high anisotropy with diffuse fast directions from the summit (Fig. 3*B*). At shallower depths (2.5 km asl; Fig. 3*A*), the localized high anisotropy extends outward to form a larger circular zone of high anisotropy with fast directions arranged radially with respect to the central low anisotropy zone. Vertical sections (Fig. 3 *C* and *D*) of the azimuthal anisotropy strength show a simpler feature: a hat-like high anisotropy feature positioned above the seismicity and uniform low anisotropy below. The checkerboard resolution test and restoration test indicate that both the fast directions and the strength of azimuthal anisotropy can be well resolved, at least at depths above 10 km bsl (*SI Appendix*, Figs. S7 and S8), so we believe these features are robust for further comparison and discussion. In fact, the distribution of anisotropy strength correlates well with the modeling results in ref. 32, which shows that the localized high anisotropy layer only exists at depths above 0 to 1 km bsl. More importantly, the 3D anisotropy strength, which indicates the spatial distribution of aligned cracks, sheds light on

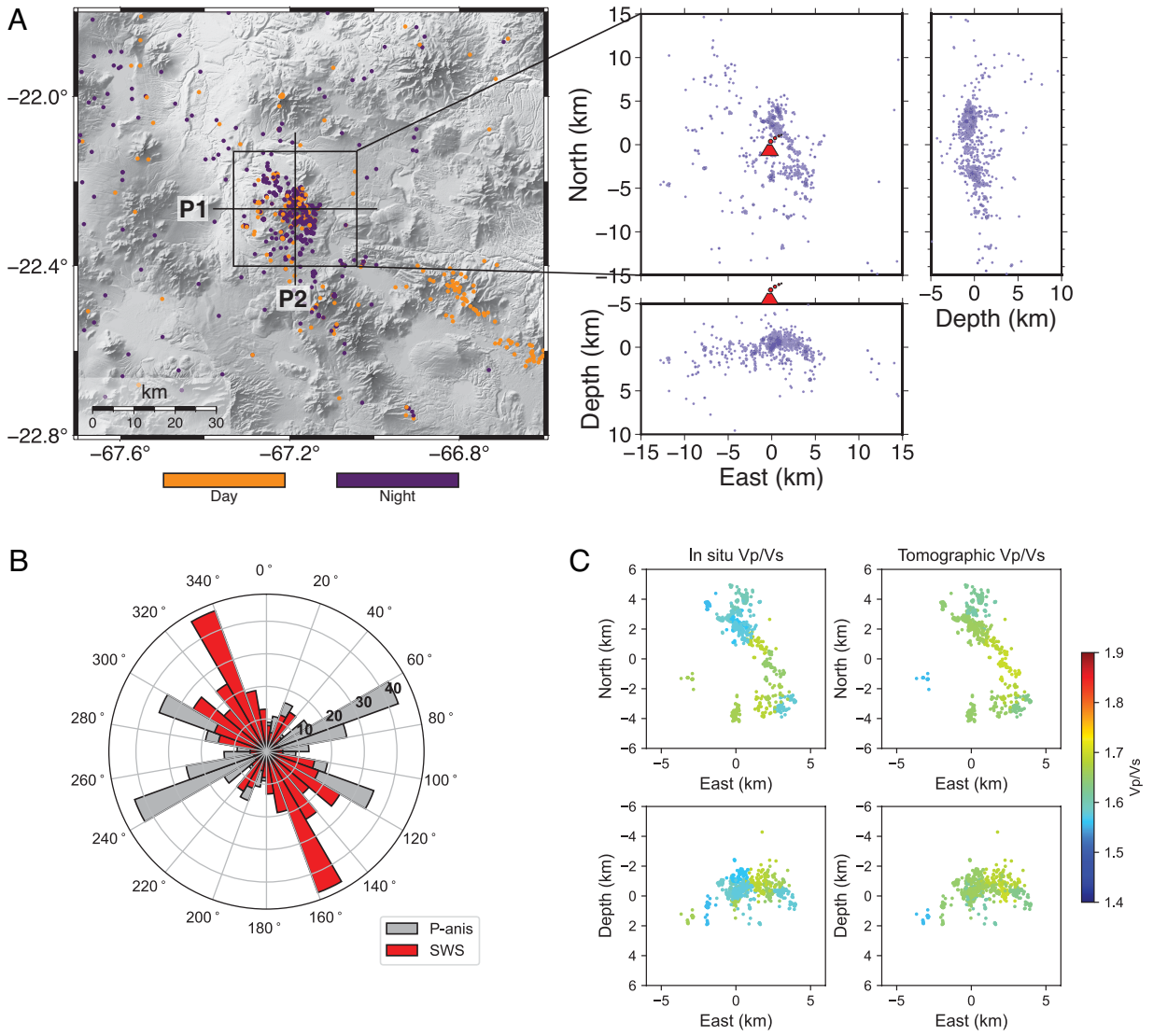

Fig. 2. Distribution of relocated earthquakes and velocity structures at Uturuncu. (*A*) *Left*: map view of day (orange) and night (purple) seismicity in the region surrounding Uturuncu; *Right*: distribution of earthquake relocations in the vicinity of the summit (marked as black box in the left panel) in map view and depth profiles along latitude and longitude across the summit. Two thick black lines indicate the locations of two vertical profiles P1 and P2 taken through the summit. (*B*) Rose diagram of fast directions from P-wave azimuthal anisotropy tomography (gray) in this study and shear wave splitting analysis (red) from ref. 32. (*C*) Horizontal and depth distribution of seismicity around the summit colored by the in situ Vp/Vs (*Left*) and the average Vp/Vs of the tomographic model (*Right*). For details of clusters and Vp/Vs values, we refer to *SI Appendix*.

the pathways of gas or fluids from shallow depth to surface. Unlike the nearly vertical pathway at depth below sea level as denoted by Region E, magma or fluids tend to migrate along open cracks outside the summit region, resulting in ring-like low Vp, low Vs, and high Vp/Vs anomalies surrounding the summit asl.

Components of the Shallow Hydrothermal System Beneath Uturuncu. To characterize the key components of Uturuncu's hydrothermal system, we integrate the findings in this study, including isotropic and azimuthal anisotropic seismic velocity structures and seismicity, with results from the recent MT inversion (20) and seismic attenuation tomography (36) of the shallow crust at Uturuncu. The distribution of Vp/Vs, azimuthal anisotropy, resistivity, and Qp/Qs along the W-E profile P1 and S-N profile P2 across the summit are shown in Fig. 4. We identify components of the system according to the combination of different geophysical properties, alongside information from geochronology, volcanology, and petrology. The features of different properties are labeled on the Vp/Vs structures in Fig. 4 and summarized in Table 1.

Crustal melting likely took place at or close to the top of the APMB as a result of transfer of magmatic heat ± hydrous fluids into the overlying crust (15). Although dacite magmas appear to have been generated close to the top of the APMB (21), there is petrological and experimental evidence for shallow pre-eruptive magma storage at pressures of 0.5 to 1.2 kb (−2.5 to 0 km bsl) and temperatures of 870 °C (45). Thus, it is likely that some unerupted plutonic equivalents of Uturuncu dacites (tonalites, granodiorites) reside at this depth, although no such rocks have been found as xenoliths in the lavas (22). Rhyolitic melt inclusions (73 to 77 wt% SiO_2) from phenocrysts in dacite lavas contain up to 3.9 wt% H_2O and up to 2,800 ppm chlorine (45). The high Cl contents are consistent with the generation of saline magmatic fluids during degassing. At the highest calculated storage pressures, the dissolved Cl content is calculated to be in equilibrium with a supercritical (single phase) fluid of salinity 2.1 wt% $NaCl_{eq}$ (46). Due to the shallow depth of the magma storage, such a fluid would undergo phase separation into a hypersaline liquid (brine) and low-salinity vapor almost immediately after exsolving from its parent magma and crossing the solvus

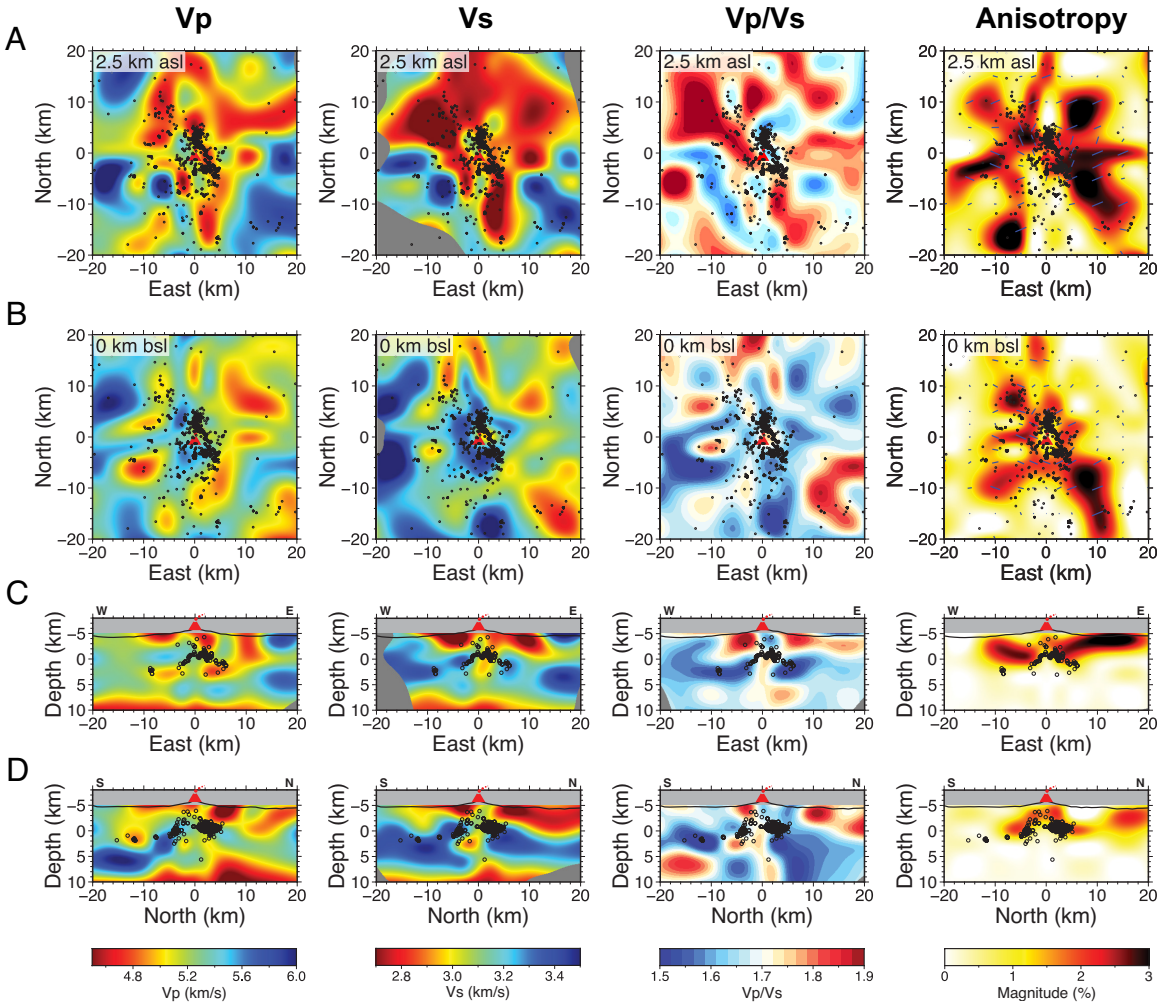

Fig. 3. Horizontal and vertical cross sections of the inverted Vp, Vs, Vp/Vs, and P-wave azimuthal anisotropy structures at (*A*) 2.5 km asl, (*B*) 0 km bsl, (*C*) profile P1 and (*D*) P2. Vertical profiles are taken through the summit as shown in Fig. 2*A*. The elevation along each vertical profile is plotted in thick black lines and the summit of Uturuncu is indicated as the red volcano symbol. Black open circles are the relocated earthquakes within ±1.25*km* to each cross section. In map view of the P-wave azimuthal anisotropy structure, the azimuth angle and length of black bars indicate the fast direction and strength of azimuthal anisotropy respectively.

(e.g., at a pressure of ~0.5 kb for a temperature of 800 °C). (47) proposed that the observed resistivity anomaly at ~0 km bsl beneath Uturuncu could be explained by just 3 vol% of brine with a salinity of 40 wt% $NaCl_{eq}$ or 15 vol% of a supercritical fluid with 5 wt% $NaCl_{eq}$ within a solid rock matrix. For comparison, 43% vol% of water-saturated rhyolite melt would be required to generate the same resistivity anomaly.

The above information provides a useful petrological framework within which to interpret our results (Fig. 4). The geophysical properties of the different components (regions) of the hydrothermal system beneath Uturuncu are summarized in Table 1 and assigned letters A-G. The relatively high Vp/Vs (≥1.7) in region E that extends from the seismogenic zone at 0 km bsl to 10 km bsl is consistent with the presence of an intergranular fluid phase, which also corresponds to the low resistivity observed in the MT inversion (20) and low Qp/Qs detected in the attenuation tomography (36). (43) proposed that a hybrid fluid phase which is composed of silicate melt exists in the lower portions of Region E and transitions to a supercritical fluid phase in the upper regions. Phase separation into a liquid brine phase and fugitive vapor (gas) phase can be expected at the top of Region E, where the lowest resistivity values occur. We interpret this region as brine-saturated porous rock as produced in the hydrodynamic models of ref. 48. Region E is therefore believed to serve as a conduit for fluids and/or melt rising from the APMB (Region D).

Above the columnar Region E, there is a region where Vp is low while Vs remains normal compared to surrounding regions, resulting in a low Vp/Vs anomaly (labeled F in Fig. 4). In geothermal systems near the water-steam transition, the presence of gas can decrease Vp while having a negligible effect on Vs, thereby producing the observed low Vp/Vs. This is also supported by the corresponding low Qp/Qs in this region (Fig. 4). We therefore interpret this region, with low Vp/Vs and low Qp/Qs, as H_2O-rich vapor that formed alongside brine through phase separation at the top of Region E and subsequently migrated further up through the conduit. In the P-wave azimuthal anisotropy images, Region F is less anisotropic than surrounding regions, indicating it is not highly fractured. Consequently, gas can be stored and is less likely to escape.

The crust surrounding regions E and F at depth above 10 km bsl comprises three horizontal layers with laterally consistent geophysical characteristics. Our interpretation of these layers is based on the crustal structure proposed by (49). Region A, the shallowest layer, has low Vp, Vs, and Vp/Vs. We attribute this layer to sedimentary rocks of likely Paleozoic age based on observations that a 3 to 4 km-thick sequence of Ordovician turbidites is reported in the northern Puna region of Argentina, 50 km due East of the study area (50). Note that this thickness is consistent with the seismic images (~4 km). Rare outcrops of folded turbidites of presumed Ordovician age also occur near the town of Quetena on the eastern flank of Uturuncu itself. The uppermost parts of

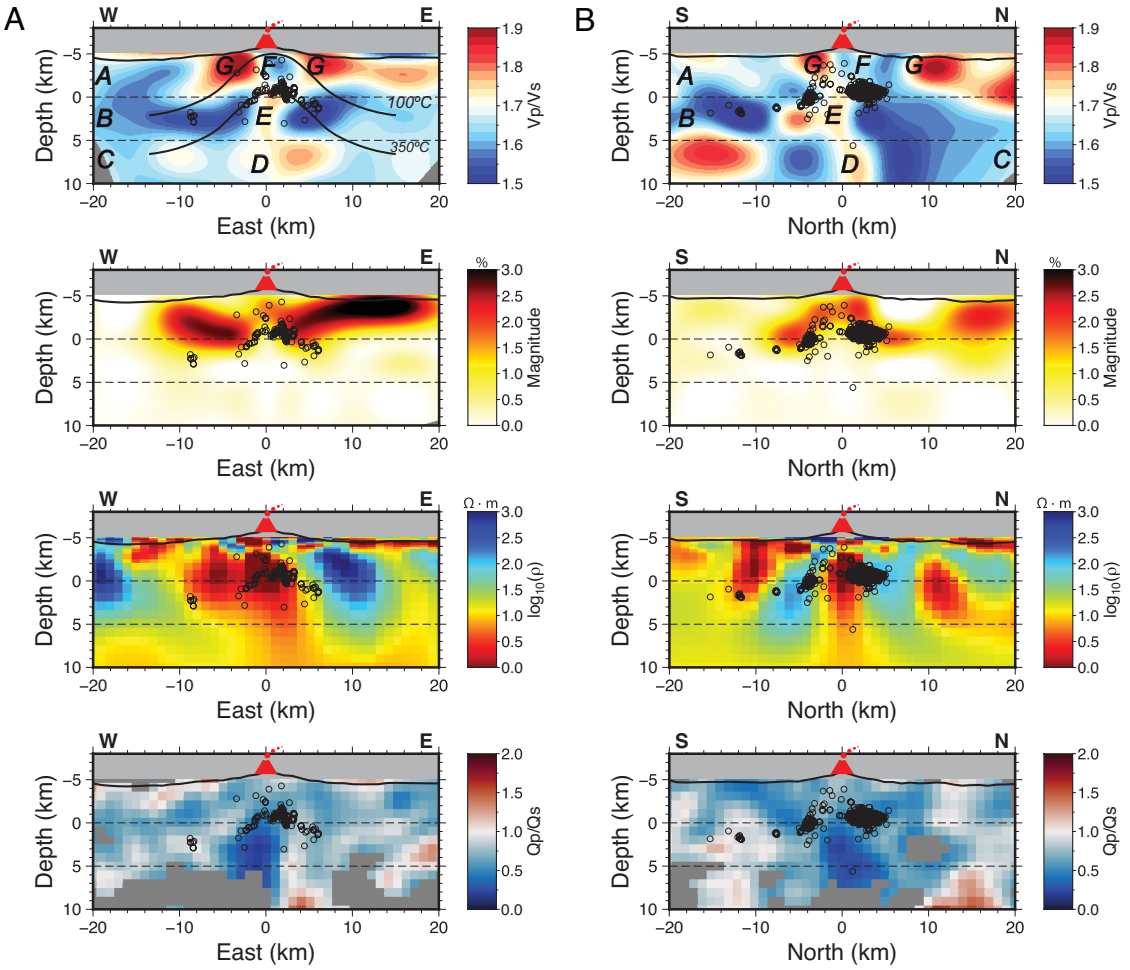

Fig. 4. Vp/Vs, azimuthal anisotropy, resistivity, and Qp/Qs structures along (*A*) West–East profile P1 and (*B*) South–North profile P2. The locations of P1 and P2 are shown in Fig. 2*A*. Italic uppercase letters on Vp/Vs panels denote the different components (regions) of the hydrothermal system beneath Uturuncu. Two curved black lines in the Vp/Vs panel of profile P1 denote the 100 °C isotherm approximating the boiling point of water and the 350 °C isotherm approximates the brittle–ductile transition, respectively. Note that the Vp/Vs and azimuthal anisotropy models are obtained in this study whereas the resistivity model is from ref. 20 and the Qp/Qs model is from ref. 36.

Region A are likely to be volcanic tuffs of the APVC. The high anisotropy of Region A suggests the presence of faults.

Beneath Region A, there lies a laterally extensive unit (Region B) with unusually low Vp/Vs (1.5 to 1.6) and negligible anisotropy. On the E-W cross section P1, Region B is confined to the depth interval of 0 to 5 km bsl but extends to 10 km bsl north of Uturuncu (cross section P2), indicating that Region B thickens northward. The low Vp/Vs is best explained by quartz- and biotite-rich metamorphic rocks such as those described elsewhere in the Altiplano (49). We suggest that Region B is a schist with composition broadly similar to the average Argentinian metasediment of (51). The estimated mineral proportions of this rock, obtained by mass balance,

Table 1. Summary of components in the shallow hydrothermal system of Uturuncu volcano

	Properties							
Region	Vp	Vs	Vp/Vs	Anisotropy	Conductivity	Qp/Qs	Seismicity	Interpretations
A	low	low	low	high	low	low	x	Thick sequence of Paleozoic sediments
B	high	high	low	low	low	low	✓	Quartz-rich schist
C	medium	medium	medium	low	medium	medium	X	Metapelitic gneiss
D	low	low	high	low	high	high	X	APMB
E	high	low	high	low	high	low	X	Melt mixed with brine and/or gas
F	low	medium	low	low-medium	high	low	✓	Gas from APMB
G	low	low	high	high	high	high	x	Fluids in highly fractured zone

Regions A-G are labeled in Figs. 4 and 6.

are 50% quartz, 30% biotite, and 20% feldspar. At 550 °C and 0.15 GPa [after (43)], the calculated seismic velocities are Vp = 5.49 km/s, Vs = 3.52 km/s, and Vp/Vs = 1.56 (52), which are consistent with our observations. The calculated density of this layer (2,730 kg/m^3) is consistent with the crustal structure in ref. 43.

The final layer (Region C), which sits directly atop the partially molten APMB (Region D, as characterized by low Vp, low Vs, high Vp/Vs, high conductivity, and high Qp/Qs), exhibits intermediate Vp, Vs, and Vp/Vs. These characteristics can be explained by a metapelitic gneiss similar to those found as xenoliths at Uturuncu [sample UT32 of (22)]. The major mineralogy of this sample is approximately sillimanite (5%) + alkali feldspar (15%) + plagioclase (21%) + cordierite (10%) + quartz (25%) ± garnet. At 650 °C and 0.3 GPa [after (43)], the calculated seismic velocities are Vp = 5.97 km/s, Vs = 3.59 km/s, and Vp/Vs = 1.66 (52), which are again in good agreement with our observations. The calculated density of this layer (2,795 kg/m^3) is also consistent with the crustal structure described in ref. 43. The higher temperature of this rock and its proximity to the APMB (Region D) indicate heating and partial melting in this zone. Thus, Region C may be the source of the crustal melting that is evident isotopically in Uturuncu dacites (23).

Finally, within Region A and immediately to the side of Region F there are two regions (G) that form an annulus. Region G has low Vp, low Vs, and high Vp/Vs, which are consistent with the presence of liquid water. We suggest that these are the condensed equivalent of the gas in Region F, which form brine lenses that can cause ground deformation (53). In this case, the boiling point curve for water is likely to pass between Regions F and G, which is consistent with the curved structure of the geotherms created by the advected heat of Region E (ref. 48). We have shown schematically two such isotherms in Fig. 4. The 100 °C isotherm approximates the boiling point of water; the 350 °C isotherm approximates the brittle–ductile transition and explains the domal shape of the seismogenic region (Fig. 2*A*).

Concentrations of Melt, Brine, and Gas in the Magmatic–Hydrothermal System in the Upper Crust. To gain a better understanding of the current state and eruption hazard at Uturuncu, we performed rock physics analysis to estimate the fluid and gas saturation for Regions E, F, and G in the shallow

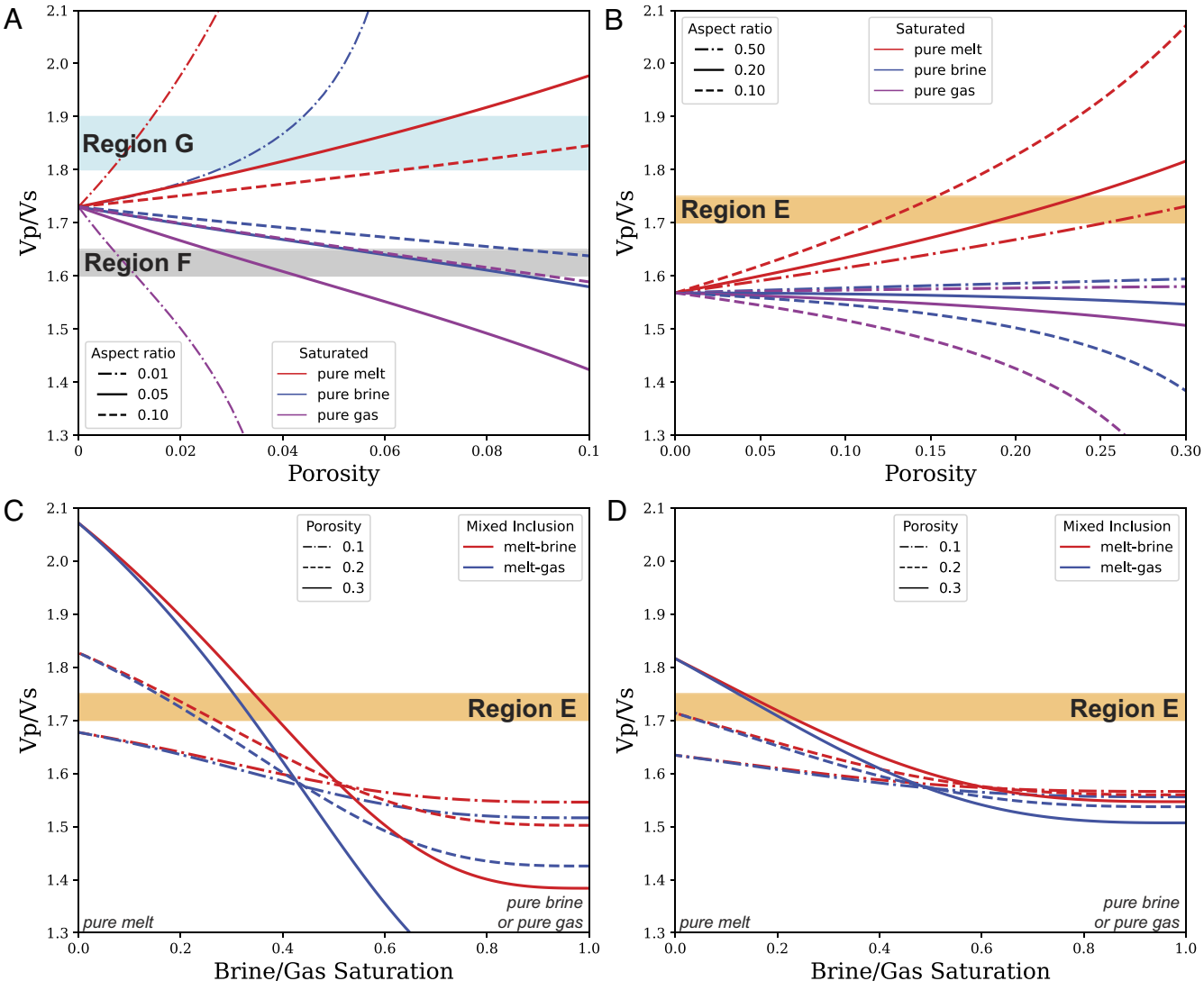

Fig. 5. Rock physics modeling of aspect ratio, porosity, and saturation in regions E, F, and G, as labeled in Fig. 4. (*A*) Estimates of aspect ratio and porosity of Regions F and G in the situation of pure melt (red line), pure brine (blue line), and pure gas (purple line) inclusion. Dash-dotted, solid, and dashed lines represent aspect ratios of 0.01, 0.05, and 0.10 as shown in the legend. (*B*) Estimates of aspect ratio and porosity of Region E in the situation of pure melt (red line), pure brine (blue line), and pure gas (purple line) inclusion. Dash-dotted, solid, and dashed lines represent aspect ratios of 0.5, 0.2, and 0.1 as shown in the legend. (*C*) Estimates of melt and brine/gas saturation in the situation of mixed inclusions when the pore aspect ratio is 0.1. Red and blue lines indicate melt-brine and melt-gas mixture, respectively. Dash-dotted, dashed, and solid lines denote porosity of 0.1, 0.2, and 0.3, respectively. (*D*) Estimates of melt and brine/gas saturation in the situation of mixed inclusions when the pore aspect ratio is 0.2. Symbols are the same as in (*C*).

magmatic–hydrothermal system by applying the Kuster–Toksöz theoretical formulations [(54), *SI Appendix*].

For Regions F and G, three types of pore-filling fluid phases ("inclusions") are considered: pure melt, pure brine, and pure gas, whose properties are listed in *SI Appendix*, Table S1. Fig. 5*A* shows the calculated effective Vp/Vs values for different inclusions with different porosities and aspect ratios. According to the results, the inclusion of pure melt increases Vp/Vs, whereas the inclusion of pure gas decreases Vp/Vs as porosity increases, especially when the aspect ratio of pores is small. For pure brine, the aspect ratio significantly affects Vp/Vs, similar to the findings of (55): when the aspect ratio is relatively large (i.e. spherical or elliptical pores), Vp/Vs decreases as porosity increases; by contrast, when the aspect ratio becomes small enough (i.e. crack shaped pores), Vp/Vs increases as porosity increases. The low Vp/Vs and relatively weak anisotropy in Region F can be explained by the presence of pure gas inclusions with porosity ranging from approximately 2.5 to 8.2% (Fig. 5*A*). Inclusions of both pure melt and pure brine with very small aspect ratios can explain high Vp/Vs and high anisotropy observed in Region G (Fig. 5*A*). However, the presence of partial melting at such shallow depths (~3 to 5 km to the surface) requires temperatures above the solidus, which is ~725 °C for water-saturated silicic systems. This is well in excess of the BDT location indicated by the seismic data (Fig. 2) and inconsistent with the geotherm of (43). For these reasons, we exclude the pure melt inclusion in Region G as a possibility. We therefore suggest that inclusion of pure brine in very thin pores (i.e. cracks) with porosity ranging from 2.7 to 4.2% is the best explanation for the high Vp/Vs and anisotropy observed in Region G.

For Region E, we consider both pure inclusions (melt, brine, or gas) and mixed inclusions (melt-brine and melt-gas) in the modeling, and assume a larger pore aspect ratio (0.1 to 0.5) as the anisotropic tomography model shows negligible anisotropy. For two-phase inclusions, "saturation" denotes the fraction of each pore that is occupied by gas or brine. In the case of pure inclusions, neither brine nor gas can account for the high Vp/Vs of Region E. For pure melt inclusions, larger porosity is required for the high Vp/Vs when pores become more spherical rather than elliptical: ~12 to 15% porosity for an aspect ratio of 0.1, ~17 to 24% porosity for 0.2, and >25% porosity for 0.5 (Fig. 5*B*). Considering that the highest melt fraction of the APMB is ~25% as estimated by (16), we assume the aspect ratio of pores in Region E is 0.1 to 0.2 for the subsequent calculations that involves mixed inclusions. For a given porosity and aspect ratio, Vp/Vs decreases as brine or gas saturation increases (Fig. 5 *C* and *D*). For aspect ratio in the range of 0.1 to 0.2, brine or gas saturation of ≤30% in either mixed melt-brine or melt-gas inclusions can explain the observed Vp/Vs at 0.2 porosity. At low brine or gas saturation, it is difficult to distinguish between melt-brine and melt-gas mixtures, suggesting that the inclusions in Region E may consist of a mixture of melt, brine, and gas.

By combining seismic tomography, petrological analysis, and rock physics modeling, we unravel the architecture of the shallow magmatic–hydrothermal system beneath Uturuncu volcano as summarized in Fig. 6 and Table 1. A high Vp/Vs column (Region E) rising from the APMB at a depth of ~10 km and cutting through metamorphic country rocks with lower Vp/Vs (Regions B and C) feeds brines and gases to the shallow surface, contributing to the dome-shaped topography of the local shallow BDT. Gases reside in the relatively weak anisotropic region beneath the summit (Region F), while brines migrate to the surrounding highly fractured areas (Region G). The migration of brines and gases from the APMB through the conduit, and the formation and collapse of brine lenses may be the source of ground deformation observed at Uturuncu. Given that the gas saturation is low (<30%) according to rock physics modeling, we propose that Uturuncu is currently at a relatively low risk of eruption.

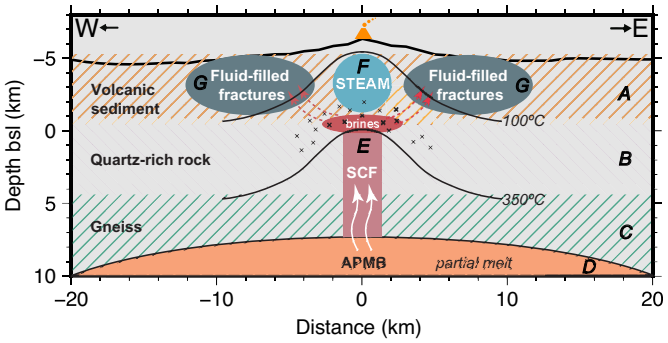

Fig. 6. Schematic E-W diagram showing the components (labeled as italic uppercase letters) of the hydrothermal system at Uturuncu. (*A*) Layer of sedimentary rocks with volcanic rocks. (*B*) Layer of quartz-rich schist with a composition broadly similar to average Argentinian metasediment. (*C*) Layer of gneiss. (*D*) APMB. (*E*) Supercritical fluids containing melt, brine, and gas. (*F*) Gas in relatively low fractured zone. (*G*) Saline fluids in highly fractured zones. Features and interpretations of Regions A-G are listed in Table 1. White arrows indicate the migration of melt, fluid, and gas ascending from the APMB. Red arrows denote the migration of brines to high fractured Region G. Note that Region B thickens north of Uturuncu extending to 10 km bsl (cross section P2 in Figs. 3 *D* and 4 *B*).

To better understand the distinctive features of the Uturuncu magmatic–hydrothermal system, here we make a detailed comparison with Campi Flegrei, Italy, a well-studied volcano that has shown noneruptive unrest in the past decades since its last eruption in 1538 (56). Table 2 summarizes the characteristics of the magmatic–hydrothermal systems at Uturuncu and Campi Flegrei. Although various types of volcanic activity have been reported at both volcanoes, they show distinctive differences in many aspects. The uplift rate at Campi Flegrei recently accelerates to ~2 cm/mo in 2024, which is accompanied by a significant increase in seismicity especially at depths above 2 km (57–59). In addition, fumarolic CO_2 flux at Campi Flegrei has increased by a factor of at least three since 2012, reaching levels comparable to those of a medium-sized erupting arc volcano in 2018 to 2019 (60). The elevated uplift rate, seismicity, and gas emissions together suggest that Campi Flegrei is currently experiencing high-level unrest. In contrast, the volcanic activity at Uturuncu is waning, as indicated by the deceleration of uplift and lower seismic activity (25, 29–31).

Similar to the low Vp/Vs in Region F at Uturuncu observed in this study, low Vp/Vs is also imaged at a depth of ~4 km beneath the clustered seismicity at Campi Flegrei, which is explained as overpressured gas-bearing rocks (62). However, at Campi Flegrei the pathway of fluid and/or gas ascent is not as well resolved as at Uturuncu (Region E in Fig. 4). At both volcanoes, a magma reservoir at mid-crustal depth is considered to be responsible for the accumulation of fluid or gas in the hydrothermal system. One notable discrepancy between the two magma reservoirs is the difference in melt fraction. The extended magma sill at 7 to 9 km depth beneath Campi Flegrei contains 65 to 75 vol% melt, which is nearly three times greater than the melt fraction in the APMB. The differences in the magmatic–hydrothermal systems of these two volcanoes, particularly the melt fraction, may be a reason for their differing levels of unrest.

Our analysis demonstrates the potential of integrating petrophysical and geophysical data in resolving the architecture of

Table 2. Summary of characteristics of the magmatic–hydrothermal systems at Uturuncu, Bolivia, and Campi Flegrei, Italy

	Uturuncu, Bolivia	Campi Flegrei, Italy
Last eruption	~ 250 ka ago (11)	Monte Nuovo eruption in 1538 (56)
Deformation	Uplift and moat of subsidence ongoing for ~50 y with variable rates of up to 1 cm/y, recently decelerate (25, 29)	Dramatic uplift of ~1.8 m during 1982 to 1984, following by several periodically slow subsidence and rapid uplift, recently accelerate in 2018, reaching rates of ~2 cm/month in 2024 (57, 58)
Degassing	Diffuse CO_2 degassing in 2009 during the PLUTONS project (15)	Fumarolic CO_2 output has grown by a factor of 3 since 2012 (60, 61)
Seismic activity	M < 3.7 seismicity beneath summit, clustered at a depth of 5 km; no increase of seismicity in 2009 to 2012 except for the triggered seismicity by the 2010 Maule earthquake (30, 31)	M < 4.2 seismicity in the central part, clustered at depths of 3 to 4 km; number of shallow earthquakes increased by a factor of >10 in 2014 (59)
Shallow hydrothermal system	Gas (low Vp/Vs) trapped below summit, with brine saturated in highly fractured zones (high Vp/Vs) above clustered seismicity at depths of 0 to 5 km	Over-pressured gas-bearing rock sequences (low Vp/Vs) at 4 km depth below clustered seismicity, with fluid-saturated at a depth of 1 km (62)
Pathway of fluids	Clearly imaged vertical conduit beneath the summit with high Vp/Vs	NOT well resolved
Deep magma reservoir	Large magma body (AMPB) at 15 to 25 km depth, with ~ 25 vol% melt (16, 20)	Extended magma sill at depths of 7 to 9 km, with 65 to 75 vol% melt (63)

magmatic–hydrothermal systems in subvolcanic crust, which is critical for volcanic hazard assessment. A better understanding of the underlying causes of the volcanic unrest and the physics of magmatic and volcanic processes requires multidisciplinary studies, as shown in this research at Uturuncu volcano.

Materials and Methods

A total of 16,153 P-wave absolute arrival times, 12,409 S-wave absolute arrival times, 86,645 P-wave catalog differential travel times, 75,160 S-wave catalog differential travel times, 19,334 P-wave WCC differential travel times, and 9,047 S-wave WCC differential travel times were selected and compiled from the ANDIVOLC and PLUTONS networks spanning the time period from April 2009 to March 2012. A multiscale inversion grid, with a minimum grid interval of 2.5 km, was utilized for seismic tomography. First, the Vp/Vs consistency-constrained DD tomography method developed by (38) was employed to obtain the isotropic Vp, Vs, and Vp/Vs models as well as the seismic event relocations. Subsequently, the P-wave azimuthal anisotropic tomography method developed by (40) was applied to determine both the fast direction and magnitude of the azimuthal anisotropy, starting from the inverted isotropic Vp model. Checkerboard tests and restoration tests were conducted to evaluate the resolutions of the inverted isotropic and anisotropic models. The in situ Vp/Vs of event clusters within 5 km of the summit was measured using the method developed by (42). Additionally, the fluid and gas saturations of the shallow hydrothermal system at Uturuncu volcano were estimated using theoretical formulations derived by (54). For further details regarding the dataset, tomographic procedures, in situ Vp/Vs measurements, and rock physics modeling, please refer to *SI Appendix*.

Data, Materials, and Software Availability. All the seismic data used in this study are available at the IRIS Data Management Center [YS (64) and XP (65) network codes, https://ds.iris.edu/ds/nodes/dmc/]. The seismic tomographic models of this work are shared via an online repository [https://doi.org/10.5281/zenodo.13759421 (66)].

ACKNOWLEDGMENTS. We thank Dr. May R. Berenbaum and two anonymous reviewers for their constructive comments that have helped to improve the manuscript. Y.L. and H.Z. were funded by the National Key Research and Development Program of China under grant 2022YFF0800701. Y.L. was funded by the National Natural Science Foundation of China under Grants 42488301 and 42004034. This work and J.M.K. and J.D.B. were funded by the NSFGEO-NERC grant NE/S008845/1. M.E.P. and P.M. were funded by NSF Grant EAR–1757495. J.D.B. was supported by a Research Professorship from the Royal Society (RP\R1\201048). The seismic instruments were provided by EarthScope Consortium through the EarthScope Primary Instrument Center at New Mexico Tech. These services are funded through the NSF Seismological Facility for the Advancement of Geoscience Award under Cooperative Agreement EAR–1724509.

Author affiliations: [a]Department of Geophysics and Planetary Sciences, School of Earth and Space Sciences, University of Science and Technology of China, Hefei 230026, Anhui, China; [b]State Key Laboratory of Precision Geodesy, University of Science and Technology of China, Hefei 230026, China; [c]Department of Earth Sciences, University of Oxford, Oxford OX1 3AN, United Kingdom; and [d]Department of Earth and Atmospheric Sciences, Cornell University, Ithaca, NY 14853

Author contributions: J.M.K. and H.Z. designed research; Y.L., J.M.K., H.Z., and J.D.B. analyzed data; Y.L., H.Z., J.D.B., M.E.P., T.H., and P.M. discussed the results and edited the paper draft; and Y.L. performed research and wrote the original draft.

The authors declare no competing interest.

1. K. V. Cashman, R. S. J. Sparks, J. D. Blundy, Vertically extensive and unstable magmatic systems: A unified view of igneous processes. *Science* **355**, eaag3055 (2017).
2. N. M. Shapiro, I. Koulakov, Probing the underbelly of a supervolcano. *Science* **348**, 758–759 (2015).
3. H. E. Huppert, A. W. Woods, The role of volatiles in magma chamber dynamics. *Nature* **420**, 493–495 (2002).
4. H.-H. Huang *et al.*, The Yellowstone magmatic system from the mantle plume to the upper crust. *Science* **348**, 773–776 (2015).
5. G. Lin, P. M. Shearer, R. S. Matoza, P. G. Okubo, F. Amelung, Three-dimensional seismic velocity structure of Mauna Loa and Kilauea volcanoes in Hawaii from local seismic tomography. *J. Geophys. Res. Solid Earth* **119**, 4377–4392 (2014).
6. R. Maguire *et al.*, Magma accumulation at depths of prior rhyolite storage beneath Yellowstone Caldera. *Science* **378**, 1001–1004 (2022).
7. J. Nakajima, A. Hasegawa, Tomographic imaging of seismic velocity structure in and around the Onikobe volcanic area, northeastern Japan: Implications for fluid distribution. *J. Volcanol. Geotherm. Res.* **127**, 1–18 (2003).
8. M. Gauntlett *et al.*, Seismic tomography of Nabro Caldera, Eritrea: Insights into the magmatic and hydrothermal systems of a recently erupted volcano. *J. Geophys. Res. Solid Earth* **128**, e2022JB025742 (2023).
9. I. Koulakov, V. Komzeleva, S. Z. Smirnov, S. B. Bortnikova, Magma-fluid interactions beneath Akutan volcano in the Aleutian arc based on the results of local earthquake tomography. *J. Geophys. Res. Solid Earth* **126**, e2020JB021192 (2021).
10. Y. Yukutake, R. Honda, M. Harada, R. Arai, M. Matsubara, A magma-hydrothermal system beneath Hakone volcano, central Japan, revealed by highly resolved velocity structures. *J. Geophys. Res. Solid Earth* **120**, 3293–3308 (2015).
11. D. D. Muir *et al.*, The temporal record of magmatism at Cerro Uturuncu, Bolivian Altiplano. *Geol. Soc. Lond. Spec. Publ.* **422**, 57–83 (2015).
12. S. L. de Silva, Altiplano-Puna volcanic complex of the central Andes. *Geology* **17**, 1102 (1989).
13. G. Zandt, M. Leidig, J. Chmielowski, D. Baumont, X. Yuan, Seismic detection and characterization of the Altiplano-Puna magma body, Central Andes. *Pure Appl. Geophys.* **160**, 789–807 (2003).

14. J. Chmielowski, G. Zandt, C. Haberland, The Central Andean Altiplano-Puna magma body. *Geophys. Res. Lett.* **26**, 783–786 (1999).
15. M. E. Pritchard *et al.*, Synthesis: PLUTONS: Investigating the relationship between pluton growth and volcanism in the Central Andes. *Geosphere* **14**, GES01578 (2018).
16. K. M. Ward, G. Zandt, S. L. Beck, D. H. Christensen, H. McFarlin, Seismic imaging of the magmatic underpinnings beneath the Altiplano-Puna volcanic complex from the joint inversion of surface wave dispersion and receiver functions. *Earth Planet. Sci. Lett.* **404**, 43–53 (2014).
17. R. del Potro, M. Díez, J. Blundy, A. G. Camacho, J. Gottsmann, Diapiric ascent of silicic magma beneath the Bolivian Altiplano. *Geophys. Res. Lett.* **40**, 2044–2048 (2013).
18. M. J. Comeau, M. J. Unsworth, F. Ticona, M. Sunagua, Magnetotelluric images of magma distribution beneath Volcán Uturuncu, Bolivia: Implications for magma dynamics. *Geology* **43**, 243–246 (2015).
19. P. MacQueen *et al.*, Dissecting a zombie: Joint analysis of density and resistivity models reveals shallow structure and possible sulfide deposition at Uturuncu volcano. *Bolivia. Front. Earth Sci.* **9**, 755 (2021).
20. M. J. Comeau, M. J. Unsworth, D. Cordell, New constraints on the magma distribution and composition beneath Volcán Uturuncu and the southern Bolivian Altiplano from magnetotelluric data. *Geosphere* **12**, 1391–1421 (2016).
21. M. Laumonier, F. Gaillard, D. Muir, J. Blundy, M. Unsworth, Giant magmatic water reservoirs at mid-crustal depth inferred from electrical conductivity and the growth of the continental crust. *Earth Planet. Sci. Lett.* **457**, 173–180 (2017).
22. R. S. J. Sparks *et al.*, Uturuncu volcano, Bolivia: Volcanic unrest due to mid-crustal magma intrusion. *Am. J. Sci.* **308**, 727–769 (2008).
23. G. Michelfelder, T. Feeley, A. Wilder, E. Klemetti, Modification of the continental crust by subduction zone magmatism and vice-versa: Across-strike geochemical variations of silicic lavas from individual eruptive centers in the Andean central volcanic zone. *Geosciences* **3**, 633–667 (2013).
24. Y. Fialko, J. Pearse, Sombrero uplift above the Altiplano-Puna magma body: Evidence of a ballooning mid-crustal diapir. *Science* **338**, 250–252 (2012).
25. S. T. Henderson, M. E. Pritchard, Time-dependent deformation of Uturuncu volcano, Bolivia, constrained by GPS and InSAR measurements and implications for source models. *Geosphere* **13**, 1834–1854 (2017).
26. M. E. Pritchard, M. Simons, An InSAR-based survey of volcanic deformation in the central Andes. *Geochem. Geophys. Geosyst.* **311**, 5 (2004).
27. J. Gottsmann, R. del Potro, C. Muller, 50 years of steady ground deformation in the Altiplano-Puna region of southern Bolivia. *Geosphere* **14**, 65–73 (2018).
28. E. Eiden, P. MacQueen, S. Henderson, M. Pritchard, Multiple spatial and temporal scales of deformation from geodetic monitoring point to active transcrustal magma system at Uturuncu volcano. Bolivia. *Geosphere* **19**, 370–382 (2023).
29. N. Lau, E. Tymofyeyeva, Y. Fialko, Variations in the long-term uplift rate due to the Altiplano-Puna magma body observed with Sentinel-1 interferometry. *Earth Planet. Sci. Lett.* **491**, 43–47 (2018).
30. T. S. Hudson, J. M. Kendall, M. E. Pritchard, J. D. Blundy, J. H. Gottsmann, From slab to surface: Earthquake evidence for fluid migration at Uturuncu volcano Bolivia. *Earth Planet. Sci. Lett.* **577**, 117268 (2022).
31. J. A. Jay *et al.*, Shallow seismicity, triggered seismicity, and ambient noise tomography at the long-dormant Uturuncu Volcano Bolivia. B*ull. Volcanol.* **74**, 817–837 (2012).
32. S. Maher, J. M. Kendall, Crustal anisotropy and state of stress at Uturuncu Volcano, Bolivia, from shear-wave splitting measurements and magnitude–frequency distributions in seismicity. *Earth Planet. Sci. Lett.* **495**, 38–49 (2018).
33. H. Mcfarlin *et al.*, Receiver function analyses of Uturuncu volcano. Bolivia and vicinity. *Geosphere* **14**, 50–64 (2018).
34. E. Kukarina *et al.*, Focused magmatism beneath Uturuncu volcano, Bolivia: Insights from seismic tomography and deformation modeling. *Geosphere* **13**, 1855–1866 (2017).
35. A. K. Farrell, S. R. McNutt, G. Thompson, Seismic attenuation, time delays, and raypath bending of teleseisms beneath Uturuncu volcano Bolivia. *Geosphere* **13**, 699–722 (2017).
36. T. S. Hudson *et al.*, Hydrothermal fluids and where to find them: Using seismic attenuation and anisotropy to map fluids beneath Uturuncu Volcano, Bolivia. *Geophys. Res. Lett.* **50**, e2022GL100974 (2023).
37. C. Alvizuri, C. Tape, Full moment tensors for small events (Mw < 3) at Uturuncu volcano Bolivia. *Geophys. J. Int.* **206**, 1761–1783 (2016).
38. H. Guo, H. Zhang, B. Froment, Structural control on earthquake behaviors revealed by high-resolution Vp/Vs imaging along the Gofar transform fault, East Pacific Rise. *Earth Planet. Sci. Lett.* **499**, 243–255 (2018).
39. H. Zhang, C. H. Thurber, Double-difference tomography:The method and its application to the Hayward fault, California. *Bull. Seismol. Soc. Am.* **93**, 1875–1889 (2003).
40. D. Eberhart-Phillips, C. M. Henderson, Including anisotropy in 3-D velocity inversion and application to Marlborough, New Zealand. *Geophys. J. Int.* **156**, 237–254 (2004).
41. Y. Liu, H. Zhang, J. M. Kendall, J. Wookey, Conjugate Fault deformation revealed by aftershocks of the 2013 Mw6.6 Lushan earthquake and seismic anisotropy tomography. *Geophys. Res. Lett.* **48**, 1–10 (2021).
42. G. Lin, P. Shearer, Estimating local Vp/Vs ratios within similar earthquake clusters. *Bull. Seismol. Soc. Am.* **97**, 379–388 (2007).
43. J. Gottsmann, J. Blundy, S. Henderson, M. E. Pritchard, R. S. J. Sparks, Thermomechanical modeling of the Altiplano-Puna deformation anomaly: Multiparameter insights into magma mush reorganization. *Geosphere* **13**, 1042–1065 (2017), 10.1130/GES01420.1.
44. J. Gottsmann, E. Eiden, M. E. Pritchard, Transcrustal compressible fluid flow explains the Altiplano-Puna gravity and deformation anomalies. *Geophys. Res. Lett.* **49**, e2022GL099487 (2022).
45. D. D. Muir, J. D. Blundy, M. C. Hutchinson, A. C. Rust, Petrological imaging of an active pluton beneath Cerro Uturuncu, Bolivia. *Contrib. Mineral. Petrol.* **167**, 980 (2014).
46. B. Tattitch, C. Chelle-Michou, J. Blundy, R. R. Loucks, Chemical feedbacks during magma degassing control chlorine partitioning and metal extraction in volcanic arcs. *Nat. Commun.* **12**, 1774 (2021).
47. A. P. Jenkins, A. C. Rust, J. Blundy, J. Biggs, Magnetotelluric investigations at Andean volcanoes: Partial melt or saline magmatic fluids? *J. Volcanol. Geotherm. Res.* **440**, 107852 (2023).
48. A. Afanasyev, J. Blundy, O. Melnik, S. Sparks, Formation of magmatic brine lenses via focussed fluid-flow beneath volcanoes. *Earth Planet. Sci. Lett.* **486**, 119–128 (2018).
49. F. Lucassen *et al.*, Composition and density model of the continental crust at an active continental margin–the Central Andes between 21° and 27°S. *Tectonophysics* **341**, 195–223 (2001).
50. H. Bahlburg, The geochemistry and provenance of Ordovician turbidites in the Argentine Puna. *Geol. Soc. Lond. Spec. Publ.* **142**, 127–142 (1998).
51. R. Becchio, F. Lucassen, S. Kasemann, G. Franz, J. G. Viramonte, Geoquímica y sistemática isotópica de rocas metamórficas del Paleozoico Inferior. Noroeste de Argentina y Norte de Chile (21–27 S). *Acta Geológica Hispánica* **34**, 273–299 (1999).
52. B. R. Hacker, G. A. Abers, Subduction Factory 3: An excel worksheet and macro for calculating the densities, seismic wave speeds, and H_2O contents of minerals and rocks at pressure and temperature. *Geochem. Geophys. Geosyst.* **5**, 2003GC000614 (2004).
53. E. Eiden, M. E. Pritchard, P. R. Lundgren, Spatial and temporal resolution needs for volcano topographic change data sets based on past eruptions (1980–2019). *Earth Space Sci.* **10**, e2023EA003054 (2023).
54. G. T. Kuster, M. N. Toksöz, Velocity and attenuation of seismic waves in two-phase media: Part I. Theoretical formulations. *Geophysics* **39**, 587–606 (1974).
55. Y. Takei, Effect of pore geometry on *VP/VS:* From equilibrium geometry to crack. *J. Geophys. Res. Solid Earth* **107**, 6–12 (2002).
56. M. A. Di Vito *et al.*, Volcanism and deformation since 12,000 years at the Campi Flegrei caldera (Italy). *J. Volcanol. Geotherm. Res.* **91**, 221–246 (1999).
57. C. Del Gaudio, I. Aquino, G. P. Ricciardi, C. Ricco, R. Scandone, Unrest episodes at Campi Flegrei: A reconstruction of vertical ground movements during 1905–2009. *J. Volcanol. Geotherm. Res.* **195**, 48–56 (2010).
58. I. Iervolino *et al.*, Seismic risk mitigation at Campi Flegrei in volcanic unrest. *Nat. Commun.* **15**, 10474 (2024).
59. F. Giudicepietro *et al.*, Insight into Campi Flegrei caldera unrest through seismic tremor measurements at Pisciarelli fumarolic field. *Geochem. Geophys. Geosyst.* **20**, 5544–5555 (2019).
60. G. Tamburello *et al.*, Escalating CO_2 degassing at the Pisciarelli fumarolic system, and implications for the ongoing Campi Flegrei unrest. *J. Volcanol. Geotherm. Res.* **384**, 151–157 (2019).
61. A. Aiuppa *et al.*, New ground-based lidar enables volcanic CO_2 flux measurements. *Sci. Rep.* **5**, 13614 (2015).
62. T. Vanorio, J. Virieux, P. Capuano, G. Russo, Three-dimensional seismic tomography from *P* wave and *S* wave microearthquake travel times and rock physics characterization of the Campi Flegrei Caldera. *J. Geophys. Res. Solid Earth* **110**, 2004JB003102 (2005).
63. A. Zollo *et al.*, Seismic reflections reveal a massive melt layer feeding Campi Flegrei caldera. *Geophys. Res. Lett.* **35**, L12306 (2008).
64. M. Pritchard, The life cycle of Andean volcanoes: Combining space-based and field studies [Data set]. International Federation of Digital Seismograph Networks. https://doi.org/10.7914/SN/YS_2009.
65. M. West, D. Christensen, Investigating the relationship between pluton growth and volcanism at two active intrusions in the central Andes [Data set]. International Federation of Digital Seismograph Networks. https://doi.org/10.7914/SN/XP_2010.
66. Y. Liu *et al.*, Seismic tomographic models in "Anatomy of magmatic hydrothermal system beneath Uturuncu volcano, Bolivia." Zenodo. https://doi.org/10.5281/zenodo.13759421.